Letters

Dynamic Reduced-Order Modeling of Wireless Power Transfer Systems Via Polynomial Approximation

Fengwei Chen, Zhipeng Deng, Hongsheng Hu, and Yue Sun

***Abstract*—This letter presents a novel method to build dynamic, control to output models for series–series compensated wireless power transfer (WPT) systems under phase or variable frequency control. In order to yield models that are as simple as necessary to explain the dominant behavior of the system, as always required in scenarios, such as control system design, a polynomial approximation technique is proposed for model order reduction. The merit of the proposed method lies in that the model order can be easily reduced to 1, 3, or 5; and models of different order can be handled in an equally simple manner. Experimental results confirm that the dynamic behavior of the system can be well modeled, even by a simple first-order model.**

***Index Terms*—Phase control, reduced-order model, variable frequency control, wireless power transfer (WPT).**

I. Introduction

WIRELESS power transfer (WPT) has received increasing attention from the community of power electronics. There are a few papers concerning the problem of dynamic modeling for WPT systems, where the primary aim is to derive a control to output model that is essential for control system design. Among the existing methods, the most well-known one could be the circuit theory-based, analytic modeling method, which is able to yield physically meaningful models, due to the use of physical laws that are known to govern the system. However, it has an obvious deficiency, i.e., the resulting model has a high order; even for the simple series–series compensated WPT system as depicted in Fig. 1, a ninth-order model will be obtained [1], [2]. To tackle this problem, there are several papers discussing how to reduce the model order with accuracy preservation. An intuitive approach is to inspect the Bode diagram of the full-order model and then, on this basis, remove the poles that are insignificant for control design, as discussed in [3]. Another approach is to approximate a resonator by a single inductor using the phasor transform theory [4], [5], then the number of reactive elements in the resonant tank can be reduced by half, so the system in Fig. 1 can be described by a reduced fifth-order model [6]. Alternatively, the modeling can be based on the coupled mode theory [7], where the main idea behind is to describe a resonator by using only two variables [8], i.e., amplitude and phase, which also results in a fifth-order model for the system in Fig. 1.

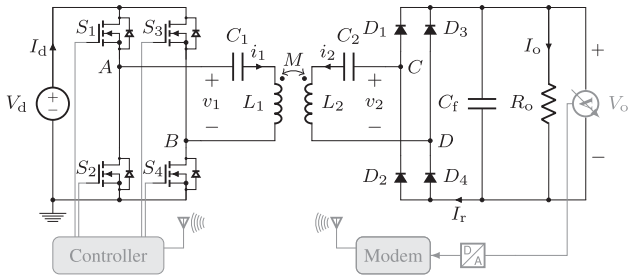

Fig. 1. Series–series compensated WPT system.

The aforementioned papers are mainly dedicated to obtaining models of specific order, so they may not allow for uniformity under different order specifications. Also, there is still a lack of discussion on the possibility to reduce the order further. As an addition to enrich the research outcome on this topic, we propose a more general method, where a polynomial approximation technique is introduced to generate reduced-order models of different order in a quite uniform manner, so avoiding additive modeling complexity when the order specification is changed. In particular, the polynomial approximation is applied to the original, complex-valued model that is derived based on circuit theory, so the final, real-valued model can be reduced to order 1, 3, or 5 after real-imaginary decomposition of the signals in the complex-valued model. Here, it should be aware that the order specification is related to the width of frequency range on which the model can accurately explain the system dynamics. Enlarging the order improves for sure the model explanatory ability on a wider range of frequencies but, at the same time, increases the model complexity. In this regard, there is a tradeoff between accuracy and complexity, which can be balanced by adjusting the order. The experimental results in Section III show that, under mild operation conditions, the dominant behavior of the WPT system can be well explained by a simple first-order model.

Manuscript received November 14, 2021; revised December 16, 2021 and January 17, 2022; accepted January 22, 2022. Date of publication January 27, 2022; date of current version March 24, 2022. This work was supported in part by the National Natural Science Foundation of China under Grants 62073246 and 62073047, and in part by the State Key Laboratory of Intelligent Control and Decision of Complex Systems. *(Corresponding author: Hongsheng Hu.)*

The authors are with the School of Automation, Chongqing University, Chongqing 400044, China (e-mail: fengwei.chen@cqu.edu.cn; 1126421395@qq.com; huhongsheng@cqu.edu.cn; syue06@cqu.edu.cn).

Color versions of one or more figures in this article are available at https://doi.org/10.1109/TPEL.2022.3146209.

Digital Object Identifier 10.1109/TPEL.2022.3146209

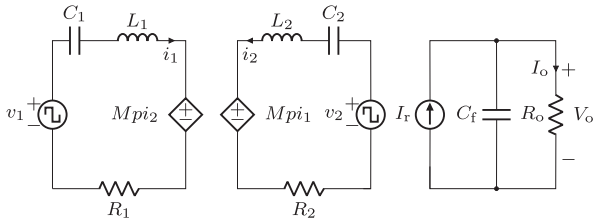

Fig. 2. Equivalent circuit of the series–series compensated WPT system.

The rest of this letter is organized as follows. The proposed reduced-order modeling method is detailed in Section II, where both large- and small-signal models are derived under phase or variable frequency control. Subsequently, experimental results are presented in Section III to validate the accuracy of the resulting large- and small-signal models. Finally, Section IV concludes this letter.

II. Reduced-Order Models

The modeling of the WPT system is based on the analysis of the equivalent circuit as shown in Fig. 2, where the dc voltage source and inverter block is replaced by a square wave voltage source, the coupling effects are replaced by two controlled voltage sources, and the diode bridge is replaced by a square wave source followed by a dc current source. From Fig. 2 and according to Kirchoff's law, the behavior of the circuit can be described by the following equations:

$$\begin{cases} Z_1(p)i_1 + Mpi_2 = v_1 \\ Z_2(p)i_2 + Mpi_1 = v_2 \\ (C_{\rm f}p + 1/R_{\rm o})\,V_{\rm o} = I_{\rm r} \end{cases} \tag{1}$$

where $Z_k(p) = L_k p + 1/(C_k p) + R_k$, $k = 1, 2$, and p is the differential operator, i.e., $p(\cdot) = d(\cdot)/dt$. Ideally, the primary and secondary resonators are designed to have the same resonant frequency, then the inductive behaviors can be canceled by the capacitor connected in series in order to minimize the impedance, thus allowing for effective power transfer.

For the modulated signals in the resonant tank, it is assumed that their envelope varies with respect to time but the rate of variation is much slower than the switching frequency of the inverter ω_0. Due to the good band-pass filtering performance of the resonant tank, the modulated signals can be approximated by their first harmonic, i.e.,

$$y = \mathrm{Re}\{Y\mathrm{e}^{j\omega_0 t}\} \tag{2}$$

where Y is the complex-valued, slowly varying envelope. Before proceeding, it is necessary to mention an important property of the differential operator p when it is applied to y

$$p^k y = \mathrm{Re}\{(p + j\omega_0)^k Y\mathrm{e}^{j\omega_0 t}\} \tag{3}$$

and it can be seen that the kth-order differentiation of y is equivalent to multiplying Y by $(p + j\omega_0)^k$.

A. Large-Signal Models

The diode bridge is a nonlinear element in the circuit. First, due to its clamping effect, v_2 is a square wave of amplitude $V_{\rm o}$ in opposite phase than i_2. Second, it converts ac signals to their dc counterparts, so the relation between $I_{\rm r}$ and i_2 can be found by reference to the conservation law. Given the amplitude of i_2

$$\begin{aligned} \|i_2\| &= \|\mathrm{Re}\{I_2\mathrm{e}^{j\omega_0 t}\}\| \\ &= \|I_{2\rm r}\cos(\omega_0 t) - I_{2\rm i}\sin(\omega_0 t)\| \\ &= \sqrt{I_{2\rm r}^2 + I_{2\rm i}^2} = |I_2| \end{aligned} \tag{4}$$

where $I_{2\rm r}$ and $I_{2\rm i}$ denote, respectively, the real and imaginary parts of I_2, it follows that:

$$v_2 \approx -\eta(V_{\rm o}, I_2)i_2 = -\frac{4V_{\rm o}}{\pi|I_2|}i_2 \tag{5a}$$

$$I_{\rm r} \approx g(I_2) = \frac{2|I_2|}{\pi}. \tag{5b}$$

The inverter converts the dc voltage to a square wave of amplitude $V_{\rm d}$, so the first harmonic approximation of the resulting square wave V_1 is

$$V_{1\rm r} \approx \lambda(U) = \frac{4V_{\rm d}}{\pi}\cos\left(\frac{U}{2}\right),\ V_{1\rm i} = 0. \tag{6}$$

Here, we have forced the imaginary part of V_1 to zero; $\cos(U/2)$ is the static input nonlinearity; and U is the phase angle between the leading and lagging legs of the full-bridge inverter.

By substitution of (5), (6), $p \leftarrow p + j\omega_0$, $i_2 \leftarrow I_2$, and $v_1 \leftarrow V_1$ into (1), we obtain a complex-valued, fifth-order polynomial model that relates the dc output $V_{\rm o}$ and phase U

$$\begin{cases} \mathcal{A}(p)I_2 = \mathcal{B}(p)\lambda(U) \\ (C_{\rm f}p + 1/R_{\rm o})\,V_{\rm o} = g(I_2) \end{cases} \tag{7}$$

where $\mathcal{A}(p) = \mathcal{D}(p) + \eta(V_{\rm o}, I_2)\mathcal{E}(p)$, and

$$\mathcal{D}(p) = Z_1(p + j\omega_0)Z_2(p + j\omega_0) - (p + j\omega_0)^2\,M^2 \tag{8a}$$

$$\mathcal{E}(p) = Z_1(p + j\omega_0) \tag{8b}$$

$$\mathcal{B}(p) = -(p + j\omega_0)M. \tag{8c}$$

Note that the order of (7) further increases to 9 after the real-imaginary decomposition of the signals in the first equation in order to obtain a real-valued model, which is too high for purposes such as control system design, so a series expansion technique is proposed in the following to reduce the order. The main idea behind is the Taylor series expansion of $\mathcal{D}(p)$, $\mathcal{E}(p)$ and $\mathcal{B}(p)$ at $p = 0$, resulting the following reduced-order polynomials:

$$D(p) = \frac{1}{\mathcal{D}_p^{(n)}}\sum_{k=0}^{n}\frac{1}{k!}\mathcal{D}_p^{(k)}p^k \tag{9a}$$

$$E(p) = \frac{1}{\mathcal{D}_p^{(n)}}\left(\mathcal{E}_p^{(0)} + \sum_{k=1}^{n-1}\frac{1}{k!}\mathcal{E}_p^{(k)}p^k\right) \tag{9b}$$

$$B(p)=\frac{1}{\mathcal{D}_p^{(n)}}\left(\mathcal{B}_p^{(0)}+\sum_{k=1}^{n-1}\frac{1}{k!}\mathcal{B}_p^{(k)}p^k\right),\ 0\leqslant n\leqslant 2 \tag{9c}$$

in which $\mathcal{D}_p^{(k)}$ is the kth-order partial derivative of $\mathcal{D}(p)$ with respect to p evaluated at $p=0$, i.e.,

$$\mathcal{D}_p^{(k)}=\left.\frac{\partial^k}{\partial p^k}\mathcal{D}(p)\right|_{p=0} \tag{10}$$

and $\mathcal{E}_p^{(k)}$, $\mathcal{B}_p^{(k)}$ are similarly defined.

The reader might feel puzzled about (9), where the Taylor series expansion is applied to polynomials defined on the differential operator p, instead of a variable. This is indeed an abuse of notations, and a more reasonable way is to formulate (9) in terms of a frequency variable. To this end, by application of Laplace transform to the modulated signal $Y(t)\mathrm{e}^{j\omega_0 t}$ defined in (2), we have

$$\mathcal{L}\{Y(t)\mathrm{e}^{j\omega_0 t}\}=Y(s-j\omega_0) \tag{11}$$

which is in fact a shifted version of $Y(s)$ to the high-frequency range before and after $j\omega_0$. If initial conditions of the signal have died out, by properties of Laplace transform, we have

$$\mathcal{L}\{p(Y(t)\mathrm{e}^{j\omega_0 t})\}=sY(s-j\omega_0). \tag{12}$$

On the other hand, if we denote $X(t)=(p+j\omega_0)Y(t)$, then

$$\mathcal{L}\{p(Y(t)\mathrm{e}^{j\omega_0 t})\}=\mathcal{L}\{X(t)\mathrm{e}^{j\omega_0 t}\}=X(s-j\omega_0). \tag{13}$$

By substitution of $s\leftarrow s+j\omega_0$ in (12) and (13), we have $X(s)=(s+j\omega_0)Y(s)$, which reveals that

$$\begin{array}{cc}\text{Time domain} & \text{Frequency domain}\\ (p+j\omega_0)^kY(t) & \leftrightarrow (s+j\omega_0)^kY(s).\end{array}$$

This mapping enables us to derive a frequency domain version (9) via the direct replacement of p by s. Then, the series expansion of the resulting polynomials at $s=0$ can be accurate if the modulation envelopes are assumed to be slowly varying, i.e., their main power is in the low-frequency range. However, as the selection of the domain of analysis does not change the final argument, we still use p in (9) in order to preserve notational consistency throughout this letter.

In the following, the detailed procedure to obtain reduced-order, large-signal models is presented.

1) First-Order Model: If $n=0$, the polynomials in (9) become scalar, herein denoted by $D(p)=1$, $E(p)=e$, and $B(p)=b$. In this case, I_2 has a static dependence on U, leading to the following first-order model:

$$\begin{cases}(1+\eta(V_\mathrm{o},I_2)e)\,I_2=b\lambda(U)\\ \dot{V}_\mathrm{o}=-\dfrac{1}{R_\mathrm{o}C_\mathrm{f}}V_\mathrm{o}+\dfrac{1}{C_\mathrm{f}}g(I_2)\end{cases} \tag{14}$$

where $\dot{V}_\mathrm{o}$ is the time derivative of V_o. Note that I_2 in the first equation of (14) should be simulated in a bootstrap manner, because it is dependent on $\eta(V_\mathrm{o},I_2)$, which in turn is a function of I_2.

2) Higher-Order Models: Higher-order models will be obtained when $n\geqslant 1$. For clarity of exposition, we reformulate the polynomials $D(p)$, $E(p)$, and $B(p)$ in descending power of p as

$$D(p)=p^n+\sum_{k=1}^{n}d_kp^{n-k} \tag{15a}$$

$$E(p)=\sum_{k=1}^{n}e_kp^{n-k},\ B(p)=\sum_{k=1}^{n}b_kp^{n-k}. \tag{15b}$$

On this basis, the first equation of (7) is reduced to order n. Below is given the reduced-order version of (7) written in state-space form

$$\begin{cases}\dot{\boldsymbol{x}}=\boldsymbol{F}\boldsymbol{x}+\boldsymbol{G}\lambda(U)\\ \dot{V}_\mathrm{o}=-\dfrac{1}{R_\mathrm{o}C_\mathrm{f}}V_\mathrm{o}+\dfrac{1}{C_\mathrm{f}}g(I_2)\end{cases} \tag{16}$$

where $\boldsymbol{x}=[x_1,\ldots,x_n]^\top\in\mathbb{C}^n$ is the state vector; $\boldsymbol{F}$ and $\boldsymbol{G}$ are model matrices in observable canonical form

$$\boldsymbol{F}=\begin{bmatrix}-a_1 & 1 & & 0\\ \vdots & 0 & \ddots & \\ \vdots & \vdots & \ddots & 1\\ -a_n & 0 & \cdots & 0\end{bmatrix},\boldsymbol{G}=\begin{bmatrix}b_1\\ \vdots\\ \vdots\\ b_n\end{bmatrix} \tag{17}$$

in which $a_k=d_k+\eta(V_\mathrm{o},I_2)e_k$. Note that, when the model matrices are parameterized in observable canonical form as in (17), the first entry of $\boldsymbol{x}$ will be I_2 (i.e., $I_2=x_1$).

By real-imaginary decomposition of the signals in (16), the real-valued, reduced-order model is obtained as

$$\begin{cases}\begin{bmatrix}\dot{\boldsymbol{x}}_\mathrm{r}\\ \dot{\boldsymbol{x}}_\mathrm{i}\end{bmatrix}=\begin{bmatrix}\boldsymbol{F}_\mathrm{r} & -\boldsymbol{F}_\mathrm{i}\\ \boldsymbol{F}_\mathrm{i} & \boldsymbol{F}_\mathrm{r}\end{bmatrix}\begin{bmatrix}\boldsymbol{x}_\mathrm{r}\\ \boldsymbol{x}_\mathrm{i}\end{bmatrix}+\begin{bmatrix}\boldsymbol{G}_\mathrm{r}\\ \boldsymbol{G}_\mathrm{i}\end{bmatrix}\lambda(U)\\ \dot{V}_\mathrm{o}=-\dfrac{1}{R_\mathrm{o}C_\mathrm{f}}V_\mathrm{o}+\dfrac{1}{C_\mathrm{f}}g(I_2).\end{cases} \tag{18}$$

B. Small-Signal Models

The large-signal models derived in the previous subsection are nonlinear in parameters, which can be linearized around an operation point to obtain linear, small-signal models. There are three nonlinear terms in the large-signal models (14) and (18): $\lambda(U)$, $g(I_2)$, and $\eta(V_\mathrm{o},I_2)$, which can be linearized as

$$\widetilde{\lambda}(U)\approx\frac{\partial}{\partial U}\lambda(U)\widetilde{U}=\lambda'\widetilde{U} \tag{19a}$$

$$\begin{aligned}\widetilde{g}(I_2)&\approx\left(\widetilde{I}_{2\mathrm{r}}\frac{\partial}{\partial I_{2\mathrm{r}}}+\widetilde{I}_{2\mathrm{i}}\frac{\partial}{\partial I_{2\mathrm{i}}}\right)g(I_2)\\ &=g_1'\widetilde{I}_{2\mathrm{r}}+g_2'\widetilde{I}_{2\mathrm{i}}\end{aligned} \tag{19b}$$

$$\begin{aligned}\widetilde{\eta}(V_\mathrm{o},I_2)&\approx\left(\widetilde{I}_{2\mathrm{r}}\frac{\partial}{\partial I_{2\mathrm{r}}}+\widetilde{I}_{2\mathrm{i}}\frac{\partial}{\partial I_{2\mathrm{i}}}+\widetilde{V}_\mathrm{o}\frac{\partial}{\partial V_\mathrm{o}}\right)\eta(V_\mathrm{o},I_2)\\ &=\eta_1'\widetilde{I}_{2\mathrm{r}}+\eta_2'\widetilde{I}_{2\mathrm{i}}+\eta_3'\widetilde{V}_\mathrm{o}\end{aligned} \tag{19c}$$

where $\widetilde{(\cdot)}$ stands for the small variation of $(\cdot)$ around a static value, and the analytical expressions of the partial derivatives are

$$\lambda' = -\frac{2V_{\rm d}}{\pi}\sin\left(\frac{U}{2}\right) \tag{20a}$$

$$\{\eta_1', \eta_2'\} = -\frac{4V_{\rm o}}{\pi|I_2|^3}\{I_{2\rm r}, I_{2\rm i}\} \tag{20b}$$

$$\{\eta_3', g_1', g_2'\} = \frac{2}{\pi|I_2|}\{2, I_{2\rm r}, I_{2\rm i}\}. \tag{20c}$$

Below, we give further details on how to derive reduced-order small-signal models.

1) First-Order Model: Letting $a = 1 + \eta(V_{\rm o}, I_2)e$ and following (19), $-aI_2 + b\lambda(U)$ can be linearized as:

$$\begin{aligned}
&-\widetilde{aI_2} + \widetilde{b\lambda}(U)\\
&\approx -a\widetilde{I}_2 - \widetilde{\eta}(V_{\rm o}, I_2)eI_2 + b\widetilde{\lambda}(U)\\
&= -a\widetilde{I}_2 - \left(\eta_1'\widetilde{I}_{2\rm r} + \eta_2'\widetilde{I}_{2\rm i} + \eta_3'\widetilde{V}_{\rm o}\right)eI_2 + b\lambda'\widetilde{U}\\
&= -a\widetilde{I}_2 + \gamma_1\widetilde{I}_{2\rm r} + \gamma_2\widetilde{I}_{2\rm i} + \gamma_3\widetilde{V}_{\rm o} + b\lambda'\widetilde{U}
\end{aligned} \tag{21}$$

in which $\gamma_k = -\eta_k' eI_2$. By real-imaginary decomposition of the signals on the left-hand side of $-\widetilde{aI_2} + \widetilde{b\lambda}(U) = 0$, we have

$$\begin{bmatrix}\gamma_{1\rm r} - a_{\rm r} & \gamma_{2\rm r} + a_{\rm i}\\ \gamma_{1\rm i} - a_{\rm i} & \gamma_{2\rm i} - a_{\rm r}\end{bmatrix}\begin{bmatrix}\widetilde{I}_{2\rm r}\\ \widetilde{I}_{2\rm i}\end{bmatrix} = -\begin{bmatrix}\gamma_{3\rm r}\\ \gamma_{3\rm i}\end{bmatrix}\widetilde{V}_{\rm o} - \begin{bmatrix}b_{\rm r}\\ b_{\rm i}\end{bmatrix}\lambda'\widetilde{U}. \tag{22}$$

Based on the $\widetilde{I}_{2\rm r}$ and $\widetilde{I}_{2\rm i}$ solved from the above equation, $\widetilde{g}(I_2)$ can be linked to $\widetilde{V}_{\rm o}$ and $\widetilde{U}$ via

$$\begin{aligned}
\widetilde{g}(I_2) &= \begin{bmatrix}g_1' & g_2'\end{bmatrix}\begin{bmatrix}\gamma_{1\rm r} - a_{\rm r} & \gamma_{2\rm r} + a_{\rm i}\\ \gamma_{1\rm i} - a_{\rm i} & \gamma_{2\rm i} - a_{\rm r}\end{bmatrix}^{-1}\\
&\quad\cdot\left(-\begin{bmatrix}\gamma_{3\rm r}\\ \gamma_{3\rm i}\end{bmatrix}\widetilde{V}_{\rm o} - \begin{bmatrix}b_{\rm r}\\ b_{\rm i}\end{bmatrix}\lambda'\widetilde{U}\right)\\
&= \vartheta_1\widetilde{V}_{\rm o} + \vartheta_2\widetilde{U}.
\end{aligned} \tag{23}$$

Finally, we are ready to present the small-signal version of (14)

$$\dot{\widetilde{V}}_{\rm o} = -\left(\frac{1}{R_{\rm o}C_{\rm f}} - \frac{\vartheta_1}{C_{\rm f}}\right)\widetilde{V}_{\rm o} + \frac{\vartheta_2}{C_{\rm f}}\widetilde{U}. \tag{24}$$

2) Higher-Order Models: As the first entry of $\boldsymbol{x}$ is I_2, $\boldsymbol{F}\boldsymbol{x} + \boldsymbol{G}\lambda(U)$ can be linearized as

$$\begin{aligned}
&\widetilde{\boldsymbol{F}\boldsymbol{x}} + \widetilde{\boldsymbol{G}\lambda}(U)\\
&\approx \boldsymbol{F}\widetilde{\boldsymbol{x}} - \widetilde{\eta}(V_{\rm o}, I_2)\begin{bmatrix}e_1 & 0 & \cdots & 0\\ \vdots & \vdots & & \vdots\\ e_n & 0 & \cdots & 0\end{bmatrix}\boldsymbol{x} + \boldsymbol{G}\widetilde{\lambda}(U)\\
&= \boldsymbol{F}\widetilde{\boldsymbol{x}} + \boldsymbol{\Gamma}_1\widetilde{\boldsymbol{x}}_{\rm r} + \boldsymbol{\Gamma}_2\widetilde{\boldsymbol{x}}_{\rm i} + \boldsymbol{\gamma}_3\widetilde{V}_{\rm o} + \boldsymbol{G}\lambda'\widetilde{U}
\end{aligned} \tag{25}$$

where

$$\boldsymbol{\Gamma}_k = -\eta_k'\begin{bmatrix}e_1 & 0 & \cdots & 0\\ \vdots & \vdots & & \vdots\\ e_n & 0 & \cdots & 0\end{bmatrix}I_2, \boldsymbol{\gamma}_k = -\eta_k'\begin{bmatrix}e_1\\ \vdots\\ e_n\end{bmatrix}I_2. \tag{26}$$

Based on (25), the small-signal version of (18) is obtained as

$$\begin{bmatrix}\dot{\widetilde{\boldsymbol{x}}}_{\rm r}\\ \dot{\widetilde{\boldsymbol{x}}}_{\rm i}\\ \dot{\widetilde{V}}_{\rm o}\end{bmatrix} = \begin{bmatrix}\boldsymbol{\Gamma}_{1\rm r} + \boldsymbol{F}_{\rm r} & \boldsymbol{\Gamma}_{2\rm r} - \boldsymbol{F}_{\rm i} & \boldsymbol{\gamma}_{3\rm r}\\ \boldsymbol{\Gamma}_{1\rm i} + \boldsymbol{F}_{\rm i} & \boldsymbol{\Gamma}_{2\rm i} + \boldsymbol{F}_{\rm r} & \boldsymbol{\gamma}_{3\rm i}\\ \frac{1}{C_{\rm f}}\boldsymbol{v}_1^\top & \frac{1}{C_{\rm f}}\boldsymbol{v}_2^\top & \frac{-1}{R_{\rm o}C_{\rm f}}\end{bmatrix}\begin{bmatrix}\widetilde{\boldsymbol{x}}_{\rm r}\\ \widetilde{\boldsymbol{x}}_{\rm i}\\ \widetilde{V}_{\rm o}\end{bmatrix} + \begin{bmatrix}\boldsymbol{G}_{\rm r}\\ \boldsymbol{G}_{\rm i}\\ 0\end{bmatrix}\lambda'\widetilde{U} \tag{27}$$

with $\boldsymbol{v}_k^\top = [1, 0, \ldots, 0]g_k'$.

C. Small-Signal Models Under Variable Frequency Control

Although Sections II-A and II-B are restricted to phase control, the proposed method of modeling can be extended to the scenario of variable frequency control without any problem. As the large-signal models under variable frequency control is completely the same than those under phase control, the attention of this subsection will be put on small-signal models.

1) First-Order Model: The frequency variable ω_0 is only involved in the coefficients of the polynomials $D(p)$, $E(p)$, and $B(p)$, so $-aI_2 + b\lambda(U)$ can be linearized as

$$-\widetilde{aI_2} + \widetilde{b\lambda}(U) = -a\widetilde{I}_2 + \gamma_1\widetilde{I}_{2\rm r} + \gamma_2\widetilde{I}_{2\rm i} + \gamma_3\widetilde{V}_{\rm o} + \alpha\widetilde{\omega}_0 \tag{28}$$

where $\alpha = -\eta(V_{\rm o}, I_2)e'I_2 + b'\lambda(U)$, with $(\cdot)' = \partial(\cdot)/\partial\omega_0$. Note that the expression (28) is similar to (21), except for the last term on the right-hand side, which is dependent on $\widetilde{\omega}_0$ instead of the previous $\widetilde{U}$. By solving $\widetilde{I}_{2\rm r}$ and $\widetilde{I}_{2\rm i}$ from $-\widetilde{aI_2} + \widetilde{b\lambda}(U) = 0$, we have

$$\begin{aligned}
\widetilde{g}(I_2) &= \begin{bmatrix}g_1' & g_2'\end{bmatrix}\begin{bmatrix}\gamma_{1\rm r} - a_{\rm r} & \gamma_{2\rm r} + a_{\rm i}\\ \gamma_{1\rm i} - a_{\rm i} & \gamma_{2\rm i} - a_{\rm r}\end{bmatrix}^{-1}\\
&\quad\cdot\left(-\begin{bmatrix}\gamma_{3\rm r}\\ \gamma_{3\rm i}\end{bmatrix}\widetilde{V}_{\rm o} - \begin{bmatrix}\alpha_{\rm r}\\ \alpha_{\rm i}\end{bmatrix}\widetilde{\omega}_0\right)\\
&= \rho_1\widetilde{V}_{\rm o} + \rho_2\widetilde{\omega}_0.
\end{aligned} \tag{29}$$

and the first-order model is

$$\dot{\widetilde{V}}_{\rm o} = -\left(\frac{1}{R_{\rm o}C_{\rm f}} - \frac{\rho_1}{C_{\rm f}}\right)\widetilde{V}_{\rm o} + \frac{\rho_2}{C_{\rm f}}\widetilde{\omega}_0. \tag{30}$$

2) Higher-Order Models: The term $\boldsymbol{F}\boldsymbol{x} + \boldsymbol{G}\lambda(U)$ can be linearized along the same light of (25) as

$$\widetilde{\boldsymbol{F}\boldsymbol{x}} + \widetilde{\boldsymbol{G}\lambda}(U) \approx \boldsymbol{F}\widetilde{\boldsymbol{x}} + \boldsymbol{\Gamma}_1\widetilde{\boldsymbol{x}}_{\rm r} + \boldsymbol{\Gamma}_2\widetilde{\boldsymbol{x}}_{\rm i} + \boldsymbol{\gamma}_3\widetilde{V}_{\rm o} + \boldsymbol{\alpha}\widetilde{\omega}_0 \tag{31}$$

where

$$\boldsymbol{\alpha} = -\begin{bmatrix}d_1'\\ \vdots\\ d_n'\end{bmatrix}I_2 - \eta(V_{\rm o}, I_2)\begin{bmatrix}e_1'\\ \vdots\\ e_n'\end{bmatrix}I_2 + \begin{bmatrix}b_1'\\ \vdots\\ b_n'\end{bmatrix}\lambda(U). \tag{32}$$

On this basis, the small-signal model is readily obtained as

$$\begin{bmatrix}\dot{\widetilde{\boldsymbol{x}}}_{\mathrm{r}}\\ \dot{\widetilde{\boldsymbol{x}}}_{\mathrm{i}}\\ \dot{\widetilde{V}}_{\mathrm{o}}\end{bmatrix}=\begin{bmatrix}\boldsymbol{\Gamma}_{1\mathrm{r}}+\boldsymbol{F}_{\mathrm{r}} & \boldsymbol{\Gamma}_{2\mathrm{r}}-\boldsymbol{F}_{\mathrm{i}} & \boldsymbol{\gamma}_{3\mathrm{r}}\\ \boldsymbol{\Gamma}_{1\mathrm{i}}+\boldsymbol{F}_{\mathrm{i}} & \boldsymbol{\Gamma}_{2\mathrm{i}}+\boldsymbol{F}_{\mathrm{r}} & \boldsymbol{\gamma}_{3\mathrm{i}}\\ \dfrac{1}{C_{\mathrm{f}}}\boldsymbol{v}_1^{\top} & \dfrac{1}{C_{\mathrm{f}}}\boldsymbol{v}_2^{\top} & \dfrac{-1}{R_{\mathrm{o}}C_{\mathrm{f}}}\end{bmatrix}\begin{bmatrix}\widetilde{\boldsymbol{x}}_{\mathrm{r}}\\ \widetilde{\boldsymbol{x}}_{\mathrm{i}}\\ \widetilde{V}_{\mathrm{o}}\end{bmatrix}+\begin{bmatrix}\boldsymbol{\alpha}_{\mathrm{r}}\\ \boldsymbol{\alpha}_{\mathrm{i}}\\ 0\end{bmatrix}\widetilde{\omega}_0 \tag{33}$$

where the state transition matrix is the same as that in (27), whereas the input matrix is different. Below are given more details on how to compute the partial derivatives in (32). According to (9) and (15), d_k has the following expression:

$$d_k=\frac{\mathcal{D}_p^{(n-k)}}{\mathcal{D}_p^{(n)}},1\leqslant k\leqslant n. \tag{34}$$

Furthermore, by the definition of $\mathcal{D}(p)$ in (8), we have

$$\frac{\partial}{\partial\omega_0}\mathcal{D}(p)=j\frac{\partial}{\partial p}\mathcal{D}(p). \tag{35}$$

These indicate that

$$d_k'=j\left(\mathcal{D}_p^{(n-k+1)}\mathcal{D}_p^{(n)}-\mathcal{D}_p^{(n-k)}\mathcal{D}_p^{(n+1)}\right)\Big/\left(\mathcal{D}_p^{(n)}\right)^2. \tag{36}$$

The above procedure can also be adopted to compute e_k' and b_k'.

D. Output Voltage Correction

Note that the power losses on the switches and diode bridge, as well as the possible errors introduced by the first-harmonic approximation, have not been taken into account in the previous modeling process, which, if considered to be significant, might introduce a bias in the model output. Here, a simple method is proposed to correct the large-signal model output

$$V_{\mathrm{o}}\leftarrow K_0+K_1V_{\mathrm{o}} \tag{37}$$

where K_0 and K_1 are the constant coefficients used to compensate for any error in the static output and static gain of the model, respectively. These coefficients can be estimated from data by solving the following least-squares fitting problem:

$$\hat{\boldsymbol{\theta}}=\arg\min_{\boldsymbol{\theta}}\left\|\mathring{V}_{\mathrm{o}}(t_k)-\boldsymbol{\phi}^{\top}(t_k)\boldsymbol{\theta}\right\|^2 \tag{38}$$

in which t_k, $k=1,\ldots,N$, is the sampling instant; $\boldsymbol{\phi}^{\top}(t_k)=[1,\mathring{V}_{\mathrm{o}}(t_k)]$ is the regression vector; $\mathring{V}_{\mathrm{o}}(t_k)$ is the true system output; and $\boldsymbol{\theta}^{\top}=[K_0,K_1]$ is the vector of the coefficients to be estimated. The solution to (38) is given as

$$\hat{\boldsymbol{\theta}}=\left(\sum_{k=1}^{N}\boldsymbol{\phi}(t_k)\boldsymbol{\phi}^{\top}(t_k)\right)^{-1}\sum_{k=1}^{N}\boldsymbol{\phi}(t_k)\mathring{V}_{\mathrm{o}}(t_k). \tag{39}$$

The effectiveness of the above bias correction technique is illustrated in Fig. 3, where the true system output data come from the second example of Section III-A ($f_{\mathrm{s}}=80$ kHz). It should be noted that the bias is only mitigated, but can not be eliminated by the proposed technique.

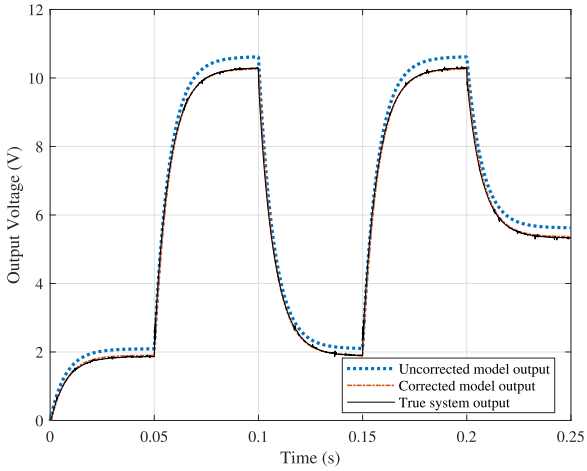

Fig. 3. Comparison of the uncorrected and corrected first-order model outputs with the true system output.

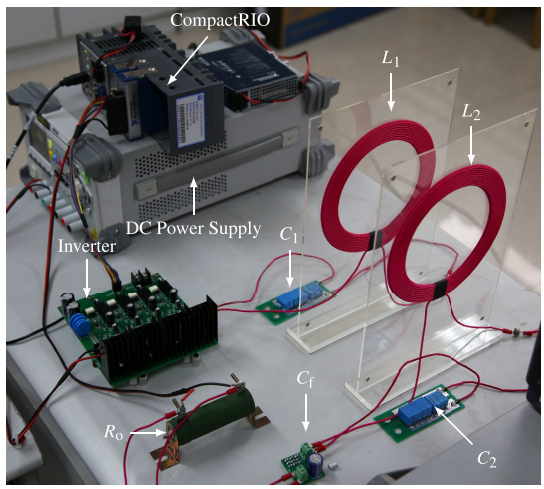

Fig. 4. Experimental apparatus.

III. Experimental Results

In this section, experimental results are presented to validate the effectiveness of the proposed modeling method. The apparatus is built based on the National Instruments (NI) CompactRIO system, with a cRIO-9030 control unit, a NI-9201 digital module, and a NI-9201 analog module; see Fig. 4. The main circuit component parameters are listed in Table I.

A. Large-Signal Models

In this section, the accuracy of the large-signal models described in Section II-A is validated; see as follows.

1) Resonant Current: The proposed reduced-order models are able to predict the envelope of the resonant current i_2. To show the accuracy of envelope prediction, the third- and fifth-order model outputs are compared with the measured i_2; see Fig. 5, where the data were generated by adding one step up and down to the phase of the inverter U. It can be seen that the fifth-order model explains very well the oscillatory nature of $|I_2|$: both the oscillating period and damping rate are correctly

TABLE I
MAIN PARAMETERS OF THE EXPERIMENTAL APPARATUS IN FIG. 4

Parameter	Explanation	Value
C_1	Capacitance of the sending resonator	38.05 nF
C_2	Capacitance of the receiving resonator	37.72 nF
C_f	Capacitance of the output filter	788 μF
f_s	Driving frequency of the inverter	80 kHz
L_1	Inductance of the sending resonator	103.80 μH
L_2	Inductance of the receiving resonator	104.45 μH
M	Mutual inductance between L_1 and L_2	7.829 μH
R_1	Equivalent resistance of the L_1, C_1 branch	160.3 mΩ
R_2	Equivalent resistance of the L_2, C_2 branch	161.5 mΩ
R_o	Load resistance	10.22 Ω
R_s	On-state resistance of the switches	12.6 mΩ
V_d	Voltage of the DC source	7 V
V_r	Forward voltage of the diodes	0.5 V

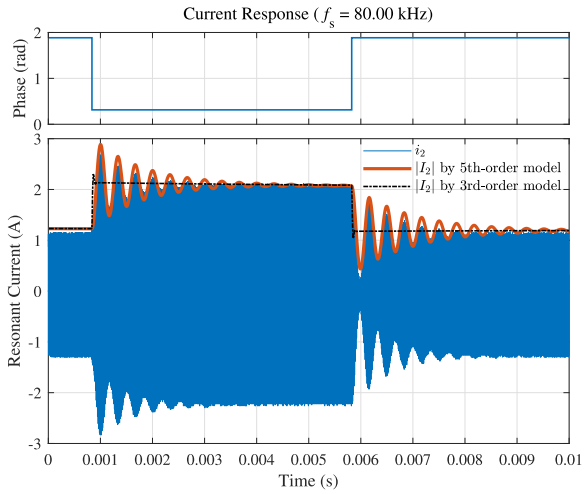

Fig. 5. Measured resonant current i_2 and its envelope $|I_2|$ predicted by third- and fifth-order models.

captured. However, there is a small bias in the steady-state value, because the power losses in the switches and diode bridge, as well as first-harmonic approximation errors, have been neglected in computing $|I_2|$. By contrast, the third-order model can not capture the oscillatory behavior, so it only gives an approximation of $|I_2|$. Interestingly, this coarse approximation does not affect too much the output voltage: the third- and fifth-order models generate identically good prediction of V_o, as will be shown in the next example, because any high-frequency content in $|I_2|$ will be smoothed by the large output capacitor and, thus, has negligible effect on the output voltage.

2) Output Voltage: In order to show how well the derived large-signal models can describe the dynamic properties of the system, the fitness ratio between the large-signal model output, V_o, and the true system output, $\mathring{V}_\mathrm{o}$, is used as the performance index to quantize the model accuracy

$$\mathrm{fit} = \left(1 - \frac{\|V_\mathrm{o} - \mathring{V}_\mathrm{o}\|_2}{\|\mathring{V}_\mathrm{o} - \mathrm{mean}\{\mathring{V}_\mathrm{o}\}\|_2}\right) \cdot 100\%. \tag{40}$$

In this example, a total number of 2500 model and true system output observations, sampled at the 10-kHz frequency, is used to compute the above performance index.

TABLE II
FITNESS RATIOS UNDER DIFFERENT SWITCHING FREQUENCIES

Model Order	Fitness Ratio		
	$f_\mathrm{s} = 81.63$ kHz	$f_\mathrm{s} = 80.00$ kHz	$f_\mathrm{s} = 78.43$ kHz
1	95.40%	97.45%	96.17%
3	94.96%	97.45%	96.06%
5	95.29%	97.13%	96.11%
9	95.29%	97.14%	96.11%

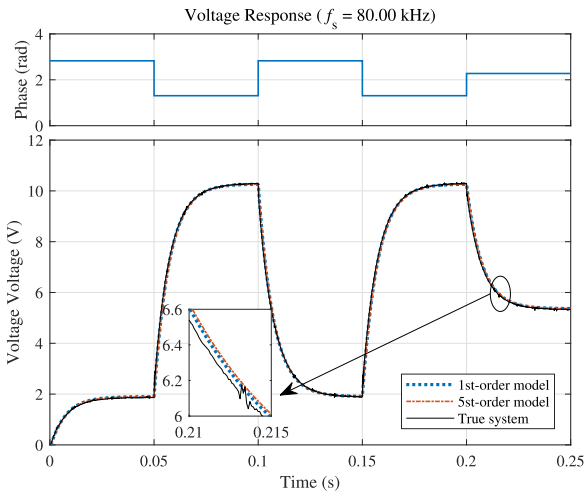

Fig. 6. Large-signal model outputs and the true system output ($f_\mathrm{s} = 80$ kHz).

The fitness ratios for the reduced first-, third-, fifth-order models obtained by using (14) and (18), as well as the full ninth-order model (see [2] for more details), are presented in Table II, while a comparison of the first- and fifth-order model outputs with the true system output is available in Fig. 6. These results show that all the reduced-order model outputs provide a reasonably good fitness to the true system output (fit $\geqslant$ 97.13% at $f_\mathrm{s} = 80$ kHz). It can further be seen that the best accuracy is achieved when the order is 1 or 3 (fit = 97.45%); whereas the value is marginally lower in the other cases, but not too much. This indicates a first-order model would be enough if the intention is on the low-frequency behavior of the system.

In practical applications, the switching frequency always deviates from the resonant frequency, due to reasons, such as aging and variation of ambient conditions. It is therefore necessary to show the performance of the proposed modeling method when there is a discrepancy between the two frequencies. The results in Table II and Fig. 7 show the accuracy of the derived models under $f_\mathrm{s} = 81.63$ and 78.43 kHz. Clearly, the fitness ratios decrease slightly but still remain good.

B. Small-Signal Models Under Phase Control

The accuracy of the small-signal models described in Section II-B is validated in frequency domain. To obtain the frequency response of the true system at a specific frequency point, a small periodic perturbation of the same frequency is injected to the system after the system has reached a steady state; then we measure the output response resulted from this perturbation and, further, apply the Fast Fourier Transform to

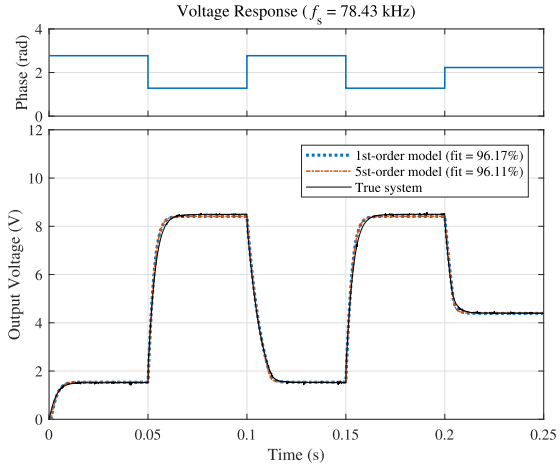

Fig. 7. Large-signal model outputs and the true system output ($f_s = 78.43$ kHz).

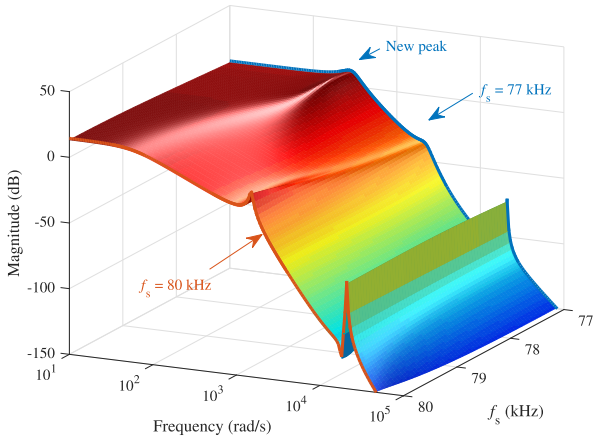

Fig. 9. Bode magnitude diagram of the ninth-order small-signal model over $f_s \in [77, 80]$ kHz.

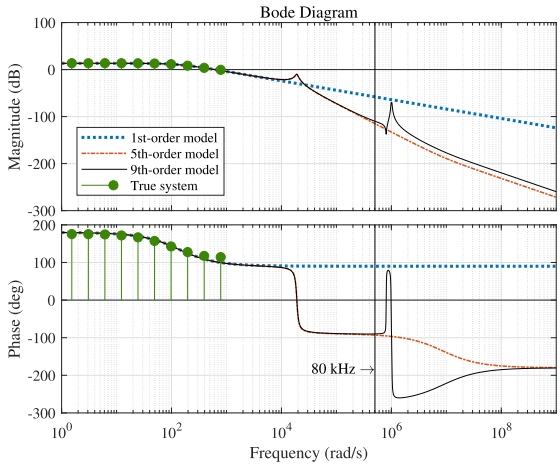

Fig. 8. Comparison of small-signal models and the true system under phase control.

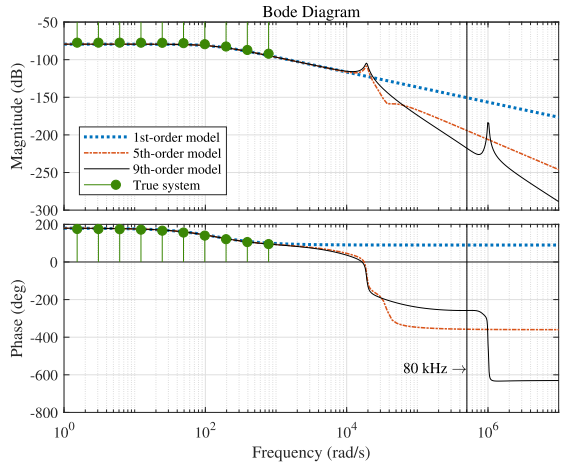

Fig. 10. Comparison of small-signal models and the true system under variable frequency control.

the time-domain input–output data; subsequently, the frequency transfer function of the true system is computed as $H(j\omega) = \widetilde{V}_o(j\omega)/\widetilde{U}(j\omega)$.

In this section, the static phase is 0.5π rad, and the perturbation around this static value is chosen as a square wave of frequency ω_T and amplitude 0.004π rad. Since we are interested in the model accuracy in the low-frequency range, ω_T is sequentially tried as $\omega_T = 250\pi/2^k$ rad/s, $k = 0, \ldots, 9$. The responses of the first-, fifth-, and ninth-order small-signal models are compared with the response of the true system at the chosen frequencies; see Fig. 8, where a perfect match among these responses can be observed, thus confirming the accuracy of the derived small-signal models.

The analytical expressions of the first- and third-order small-signal models in transfer function form, derived according to (24) and (27), respectively, are given as follows:

$$\widetilde{V}_o = \frac{-647.7}{p + 136.9}\widetilde{U}$$

$$\widetilde{V}_o = \frac{-3.414 \cdot 10^7 p - 7.278 \cdot 10^{12}}{p^3 + 1.064 \cdot 10^5 p^2 + 1.125 \cdot 10^{10} p + 1.538 \cdot 10^{12}}\widetilde{U}.$$

Fig. 9 shows some interesting results on how the Bode diagram evolves when the switching frequency f_s is drifting from the nominal value (U is fixed as 0.5π rad during this drifting process). It can be seen that a new peak emerges at a relatively higher frequency point ($\omega \approx 1382$ rad/s) when f_s reduces to 77 kHz. Due to the enlarged system bandwidth, it is then not hard to understand why the output response in Fig. 7 is quicker when the switching frequency is reduced to 78.43 kHz, in comparison to the 80-kHz case in Fig. 6.

C. Small-Signal Models Under Variable Frequency Control

The small-signal models derived under variable frequency control are validated in the same way as that in Section III-B. To acquire the frequency response of the true system, the switching frequency f_s is perturbed by a square wave of amplitude 0.32 kHz around the static value of 80.32 kHz, while the phase of the inverter is fixed as $U = 0.5\pi$ rad. Again, the frequency points to be tested are chosen as $\omega_T = 250\pi/2^k$ rad/s, $k = 0, \ldots, 9$. The comparison results are presented in Fig. 10, which confirm again the high accuracy of the derived small-signal models.

Finally, we present the first- and third-order transfer function models that are derived, respectively, according to (30) and (33)

$$\widetilde{V}_{\rm o} = \frac{-0.01497}{p+139.5}\widetilde{\omega}_0$$

$$\widetilde{V}_{\rm o} = \frac{-1.12\cdot 10^4 p - 5.903\cdot 10^8}{p^3 + 3.644\cdot 10^5 p^2 + 3.949\cdot 10^{10} p + 5.503\cdot 10^{12}}\widetilde{\omega}_0.$$

IV. Conclusion

The problem of reduced-order modeling of series–series compensated WPT systems in input–output form has been investigated. The proposed method for model order reduction is based on low-order Taylor series expansion, which has shown to be simple yet effective when the main objective is to model the low-frequency behavior of the system. We have performed order reduction to the original complex-valued model derived based on circuit theory, which, after order reduction and real-imaginary decomposition of the signals in the model, can be converted to a real-valued model of order 1, 3, or 5. Experiments have confirmed the high accuracy of the large-signal models in time domain: they all yield a fitness ratio greater than 97.13% at the 80-kHz switching frequency under phase control; and that the small-signal model responses coincide very well with the true system response, in the low-frequency range up to 250π rad/s.

References

[1] Q. Deng *et al.*, "Modeling and control of inductive power transfer system supplied by multiphase phase-controlled inverter," *IEEE Trans. Power Electron.*, vol. 34, no. 9, pp. 9303–9315, Sep. 2019.

[2] F. Chen, H. Garnier, Q. Deng, M. K. Kazimierczuk, and X. Zhuan, "Control-oriented modeling of wireless power transfer systems with phase-shift control," *IEEE Trans. Power Electron.*, vol. 35, no. 2, pp. 2119–2134, Feb. 2020.

[3] H. Feng and S. M. Lukic, "Reduced-order modeling and design of single-stage LCL compensated IPT system for low voltage vehicle charging applications," *IEEE Trans. Veh. Technol.*, vol. 69, no. 4, pp. 3728–3739, Apr. 2020.

[4] S. Lee, B. Choi, and C. T. Rim, "Dynamics characterization of the inductive power transfer system for online electric vehicles by laplace phasor transform," *IEEE Trans. Power Electron.*, vol. 28, no. 12, pp. 5902–5909, Dec. 2013.

[5] J. Qu and C. K. Lee, "Dynamic modeling for the wireless power transfer system in domino structure," *IEEE Trans. Ind. Electron.*, vol. 69, no. 4, pp. 3556–3565, Apr. 2022.

[6] H. Li, J. Fang, and Y. Tang, "Dynamic phasor-based reduced-order models of wireless power transfer systems," *IEEE Trans. Power Electron.*, vol. 34, no. 11, pp. 11361–11370, Nov. 2019.

[7] A. Kurs, A. Karalis, R. Moffatt, J. D. Joannopoulos, P. Fisher, and M. Soljačić, "Wireless power transfer via strongly coupled magnetic resonances," *Science*, vol. 317, no. 83, pp. 83–86, 2007.

[8] H. Li, K. Wang, L. Huang, W. Chen, and X. Yang, "Dynamic modeling based on coupled modes for wireless power transfer systems," *IEEE Trans. Power Electron.*, vol. 30, no. 11, pp. 6245–6253, Nov. 2015.